remote sensing

MDPI

Article

The Role of Emissivity in the Detection of Arctic Night Clouds

Filomena Romano [1,*], Domenico Cimini [1,2], Saverio T. Nilo [1], Francesco Di Paola [1], Elisabetta Ricciardelli [1], Ermann Ripepi [1] and Mariassunta Viggiano [1]

[1] Institute of Methodologies for Environmental Analysis, National Research Council (IMAA/CNR), Potenza 85100, Italy; domenico.cimini@imaa.cnr.it (D.C.); saverio.nilo@imaa.cnr.it (S.T.N.); francesco.dipaola@imaa.cnr.it (F.D.P.); elisabetta.ricciardelli@imaa.cnr.it (E.R.); ermann.ripepi@imaa.cnr.it (E.R.); mariassunta.viggiano@imaa.cnr.it (M.V.)

[2] Center of Excellence Telesensing of Environment and Model Prediction of Severe events (CETEMPS), University of L'Aquila, L'Aquila 67100, Italy

* Correspondence: filomena.romano@imaa.cnr.it; Tel.: +39-0971-427266

Academic Editors: Richard Müller and Prasad S. Thenkabail
Received: 13 February 2017; Accepted: 22 April 2017; Published: 26 April 2017

Abstract: Detection of clouds over polar areas from satellite radiometric measurements in the visible and IR atmospheric window region is rather difficult because of the high albedo of snow, possible ice covered surfaces, very low humidity, and the usual presence of atmospheric temperature inversion. Cold and highly reflective polar surfaces provide little thermal and visible contrast between clouds and the background surface. Moreover, due to the presence of temperature inversion, clouds are not always identifiable as being colder than the background. In addition, low humidity often causes polar clouds to be optically thin. Finally, polar clouds are usually composed of a mixture of ice and water, which leads to an unclear spectral signature. Single and bi-spectral threshold methods are sometimes inappropriate due to a large variability of surface emissivity and cloud conditions. The objective of this study is to demonstrate the crucial role played by surface emissivity in the detection of polar winter clouds and the potential improvement offered by infrared hyperspectral observations, such as from the Infrared Atmospheric Sounding Interferometer (IASI). In this paper a new approach for cloud detection is proposed and validated exploiting active measurements from satellite sensors, i.e., the CloudSat cloud profiling radar (CPR) and the Cloud-Aerosol Lidar with Orthogonal Polarization (CALIOP) on board the Cloud-Aerosol Lidar and Infrared Pathfinder Satellite Observations (CALIPSO). For a homogenous IASI field of view (FOVs), the proposed cloud detection scheme tallies with the combined CPR and CALIOP product in classifying 98.11% of the FOVs as cloudy and also classifies 97.54% of the FOVs as clear. The Hansen Kuipers discriminant reaches 0.95.

Keywords: cloud detection; arctic night; surface emissivity

1. Introduction

The advent of new satellite observations promises to transform cloud-climate studies [1], especially in the polar regions [2]. Satellite observations are currently exploited to improve cloud parameterization in climate models [3], to measure cloud occurrence and persistence [4], and to study cloud-surface interactions [5]. An important reason for improving satellite cloud detection methods is that many remote sensing applications require clear skies in order to work accurately (e.g., sea surface temperature retrievals, ocean colour retrievals, surface albedo retrievals, snow and sea ice mapping). In addition, the magnitude of Arctic warming depends on cloud climatology greatly, as Arctic clouds exert a strong influence on the underlying surface and the Arctic climate in general [6]. Even the presence of thin cirrus clouds, if undetected, can impact radiative transfer calculations significantly. Cirrus clouds

are crucially important to the global radiative process and the thermal balance of the Earth, allowing solar heating while reducing infrared radiation cooling to space. The radiation balance in the polar regions is yet to be understood due to the lack of accurate cloud climatology [7–9]. This is mostly because of the difficulty in detecting clouds by passive satellite sensors over snow and ice surfaces, where it is difficult to distinguish between the reflectance and temperature of clouds and those of the underlying surface [2,10]. A further difficulty in polar regions is the false identification of clouds due to polar atmospheric temperature inversions, which causes clouds to be even warmer than the underlying snow or ice surface. This paper focuses on the Arctic region, which is still poorly covered by conventional meteorological sounding, due to the hostile environment. The high spectral resolution of advanced infrared sensors can significantly improve temperature and moisture soundings if compared with the other operational retrievals. Infrared observations, however, are frequently affected by the presence of clouds in the field of view (FOV). Thus, observations must be processed for operational data assimilation and inversion of geophysical parameters by screening the cloud-contaminated soundings. Polar-orbiting satellites provide frequent overpasses on the Arctic area with sufficient spatial resolution; nevertheless, cloud detection and parameter retrieval are still very difficult at high latitudes. Most of the Arctic surface is covered with snow and ice, which reduces the visible contrast between clouds and surface. In addition, during the winter there is little solar contribution, therefore techniques based on reflectance in the visible and near infrared (e.g., 1.6 μm channel) are not applicable. Moreover, Arctic clouds are often low and thin and composed of mixtures of ice and water [7]. Over most surface types, visible/infrared (VIS/IR) threshold techniques are generally sufficient to detect clouds since they are both brighter and colder than the surface. For example, a FOV is identified as cloudy when its visible reflectance is 3% higher than the reflectance of the surrounding FOVs and its brightness temperature (BT) is 3 °C lower than the BT of the surrounding FOVs [11]. However, threshold methods experience difficulties in the Arctic region stemming from low-to-no contrast between clouds and underlying snow–sea ice surface in the visible reflectances and the IR brightness temperatures [12–15].

As such, uncertainties related to surface emissivity play an important role, since spectral emissivity for ice/snow surfaces may differ significantly depending upon microphysical properties. Furthermore, in particular cases the spectral emissivity of ice/snow surfaces may resemble the spectral signatures of clouds when observed by satellite and could potentially confuse detection techniques relying on thresholds. This in particular affects the infrared (IR) window tests usually exploited in cloud detection schemes over the Arctic region [16–18]. Indeed, global validation of satellite cloud detection demonstrated the poorest performances over the polar regions during winter [15,19]. Therefore, much effort has been spent lately in improving cloud detection in the Arctic [20,21]. It follows that the vast majority of improvements over earlier cloud mask algorithm concern nighttime scenes, including polar night [22,23]. Nowadays, current operational cloud detection algorithms exploit more sophisticated procedures for detecting polar night-time clouds, including dynamic thresholds, ancillary data, and snow and ice identification [24–26]. Recently, the availability of ultrasensitive day/night band channels in the visible/near-infrared range [27], capable of measuring extremely low light such as reflected moonlight, stimulated the development of new nighttime lunar cloud properties algorithms [28].

In this study, we analyse the spectrally-resolved radiance over an Arctic area to detect cloud contamination in the sensor FOV. Over the last few years meteorological satellites have carried infrared sensors with very high spectral resolutions. The spectral radiances of these new sensors contain the fingerprint of the underlying emitting surface, which may be used both to estimate the emissivity and identify the presence of clouds over peculiar surfaces, e.g., a desert [29].

Section 2 describes the instruments and data description. The effect of sea/ice/snow emissivity spectra on simulated radiances in the IR wavenumber range often used for cloud detection (750–1000 cm^{-1}) is studied in Section 3. Section 4 reports the impact of surface emissivity uncertainties on the performances of polar night-time cloud detection techniques based on hyperspectral observations and a possible improvement to polar cloud detection methods. Finally, a validation of the described method is reported in Section 5, using the combined CPR and CALIOP products

(2B-GEOPROF-LIDAR) distributed by the CloudSat data processing centre (http://cloudsat.atmos.colostate.edu/).

2. Instruments and Data Description

The Infrared Atmospheric Sounding Interferometer (IASI) consists of a Fourier Transform Spectrometer based on a Michelson Interferometer [30]. The instrument provides spectra of high radiometric quality at 0.5 cm^{-1} resolution, from 645 to 2760 cm^{-1}. Data samples are taken at intervals of 25 km along and across the track, each sample having a maximum diameter of about 12 km. IASI is a key payload element of the Meteorological Operational satellite (MetOp) series of European meteorological polar-orbit satellites [31]. IASI has been designed for operational meteorological soundings with a very high level of accuracy being devoted to improved medium range weather forecast. The temperature is measured under clear sky with a vertical resolution of 1 km in the lower troposphere, a horizontal resolution of 25 km, and an accuracy of 1 K. The humidity is measured under clear sky with a vertical resolution of 1–2 km in the lower troposphere, a horizontal resolution of 25 km, with an accuracy of 10%. It is also designed for atmospheric chemistry observations, aimed at estimating and monitoring trace gases like ozone, methane, or carbon monoxide on a global scale [30].

The Advanced Very High Resolution Radiometer (AVHRR/3) is one of the instruments provided by the U.S. National Oceanic and Atmospheric Administration (NOAA) to fly on MetOp-A. The AVHRR/3 scans the Earth surface in six spectral bands in the range of 0.58–12.5 μm. The instrument has an instantaneous FOV of 1.3 milliradians providing a nominal spatial resolution of 1.1 km at nadir. (http://noaasis.noaa.gov/NOAASIS/ml/avhrr.html).

The Moderate–Resolution Imaging Spectroradiometer (MODIS) is an instrument of the Earth Observing System (EOS) and it measures radiances at 36 wavelengths (from 0.4 to 14.5 μm) at 250 m spatial resolution in two visible bands, 500 m resolution in five visible bands, and 1000 m resolution in the infrared bands [22,32].

CloudSat is an experimental satellite that uses radar to observe clouds and precipitation from space. The Cloud Profiling Radar (CPR), the main instrument on CloudSat, is a 94 GHz radar providing vertically-resolved information on cloud location, cloud ice and liquid water content, precipitation, cloud classification, radiative fluxes, and heating rates [33]. The vertical resolution is 480 m with 240 m sampling, and the horizontal resolution is approximately 1.4 km (cross-track) × 2.5 km (along-track) with sampling roughly every 1 km. Range bins with detectable hydrometeors are reported in the 2B-GEOPROF product [34]. A cloudy range bin is associated with a confidence mask value that ranges from 0–40. Values $\geq$30 are confidently associated with clouds although values as low as six suggest clouds approximately 50% of the time [35].

The Cloud-Aerosol Lidar and Infrared Pathfinder Satellite Observation (CALIPSO) payload consists of three nadir-viewing instruments: the Cloud-Aerosol Lidar with Orthogonal Polarization (CALIOP), the imaging infrared radiometer (IIR), and the wide field camera (WFC) [36]. This instrument synergy enables the retrieval of a wide range of aerosol and cloud products including: vertically-resolved aerosol and cloud layers, extinction, optical depth, aerosol and cloud type, cloud water phase, cirrus emissivity, and particle size and shape [36,37]. The horizontal resolution is 70 m with an instantaneous field of view (IFOV) sampled at 333 m intervals along the track, and the vertical resolution is 30 m.

A combined radar-lidar product (2B-GEOPROF-LIDAR) is available [35]. The 2B-GEOPROF-LIDAR algorithm is designed to extract maximum information from the combined radar and lidar sensors in order to provide the best description of the occurrence of hydrometeor layers in the vertical column. The CPR radar and CALIPSO lidar provide complementary information regarding the occurrence of hydrometeor layers in the vertical column. The radar penetrates optically thick layers that attenuate the lidar signal, and it observes layers of cloud-free precipitation that may not be observed by the lidar. The lidar senses tenuous hydrometeor layers that are below the detection threshold of the radar, e.g., the top of optically thin ice cloud layers that the radar would miss, and with higher spatial

resolution than the radar. Note that CloudSat and CALIPSO are active instruments and consequently do not suffer from the same passive instrument retrieval challenges over bright and cold surfaces [3]. Since the two instruments have different features such as vertical resolution, spatial resolution, and spatial frequency, the spatial domain of the output products of this algorithm is defined in terms of the spatial grid of the CPR. The GEOPROF-LIDAR swath data include the cloud fraction, the number of hydrometeor layers, the height of layer base, the height of layer top, and the contribution flag for each layer base and top.

3. Emissivity and Simulated IASI Data

3.1. Observed Arctic Emissivity Spectra

Arctic regions are characterized by different surface types, such as land, ice, snow, and sea-water, having significantly different infrared spectral emissivity (ξ_λ), due to their intrinsic microphysical properties. Furthermore, even for the same surface type there may be discrepancies because of other effects including, but not limited to, surface roughness, impurities, grain size, and wetness.

Infrared spectral emissivity was measured for a large variety of natural materials at the Institute for Computational Earth System Science (ICESS) of the University of California in Santa Barbara (UCSB) [38], and are available on the UCSB Emissivity Library web site (http://www.icess.ucsb.edu/modis/EMIS/html/em.html). The observing angle used to measure these emissivity spectra is 10 degrees off nadir. In this study, we consider the UCSB emissivity spectra for ice, snow, and sea-water, as illustrated in Figure 1. Significant differences in spectral emissivity are evident in the 750–1000 cm^{-1} range, where ξ_λ differ by 5–6% for ice, snow, and sea-water surfaces.

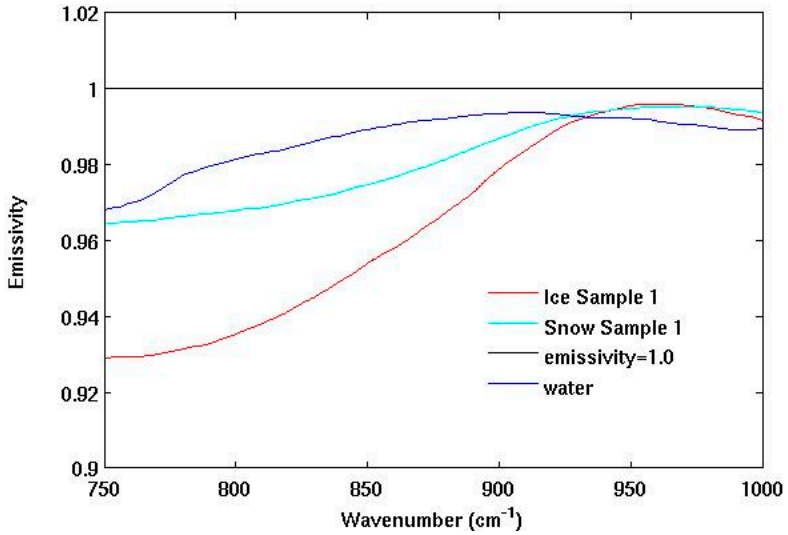

Figure 1. Spectral emissivity for cases of sea-water, ice, and snow surfaces (data from the MODIS UCSB Emissivity Library).

Due to the spectral features in the 750–1000 cm^{-1} range, uncertainties in ξ_λ play an important role in cloud detection. In fact, a test often used in cloud detection algorithms relies on the differential absorption of ice and liquid water in the 833–1111 cm^{-1} range, as illustrated by the absorption coefficient spectra in Figure 2 [17,18,20].

Accordingly, the difference between observations at 833.33 cm^{-1} and 909.09 cm^{-1} was demonstrated to be indicative of cloud presence [17,18,20].

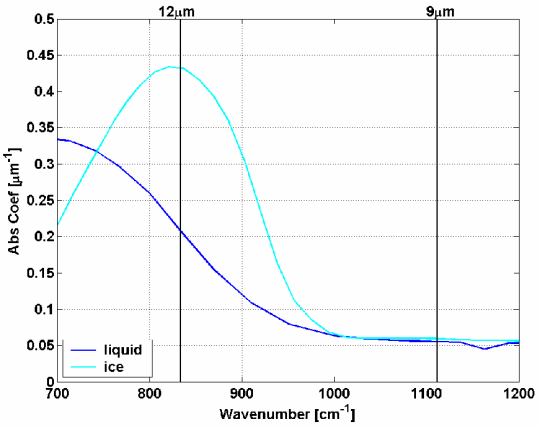

Figure 2. Liquid and solid water absorption coefficient spectra (after Hale and Querry [39], and Warren [40]).

3.2. Simulated Clear-Sky IASI Spectra

High resolution IASI radiance spectra are simulated by processing a set of 305 polar temperatures and humidity profiles, selected from the Thermodynamic Initial Guess Retrieval (TIGR) dataset [41] and from radiosondes launched during the Arctic Water Vapor Intensive Operational Period 2004 [42] from the Atmospheric Radiation Measurement Program [43] North Slope of Alaska site [44], in order to study the effect on ξ_λ of cloud detection algorithms.

The radiative transfer model used for clear sky simulation is the Line-By-Line Radiative Transfer Model (LBLRTM) [45]. Figures 3 and 4 show selected IASI spectra simulated using the TIGR temperature and humidity profiles shown in Figure 5 and the ice and sea-water surface emissivities in Figure 1. As expected, the simulated spectra in Figure 3 show significantly different slopes in the 750–1000 cm^{-1} range with respect to those in Figure 4, despite the same temperature and humidity profiles, demonstrating the impact of the different surface emissivities. The spectral features of emissivity clearly cause the simulated brightness temperatures to significantly vary in the 750–1000 cm^{-1} range; differences as large as 2.5 K are imputable uniquely to the surface emissivity, as there is no cloud involved in these simulated spectra.

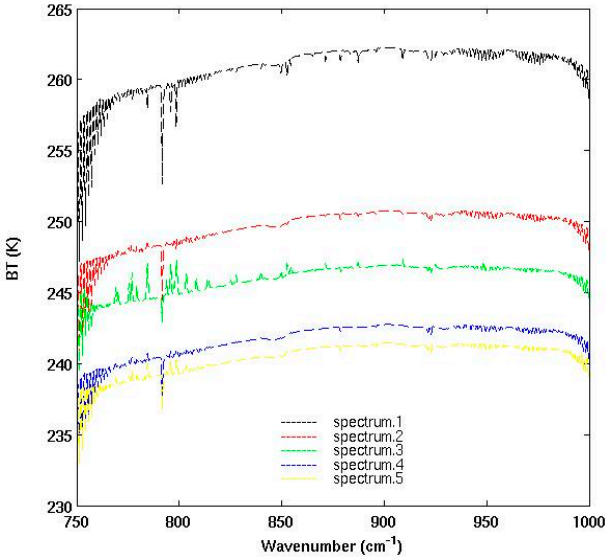

Figure 3. Infrared Atmospheric Sounding Interferometer (IASI) brightness temperature simulations in clear-sky using spectral emissivity of the ice surface and the atmospheric profiles in Figure 5.

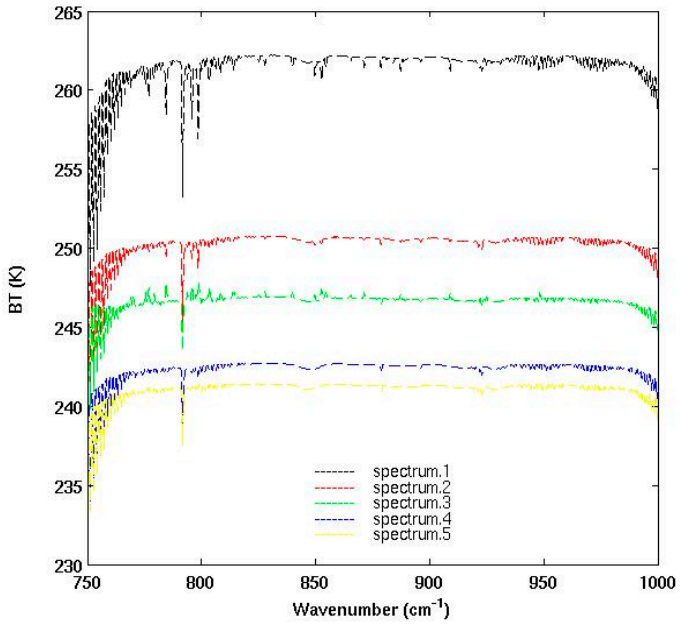

Figure 4. IASI brightness temperature simulations in clear-sky using spectral emissivity of the sea-water surface and the atmospheric profiles in Figure 5.

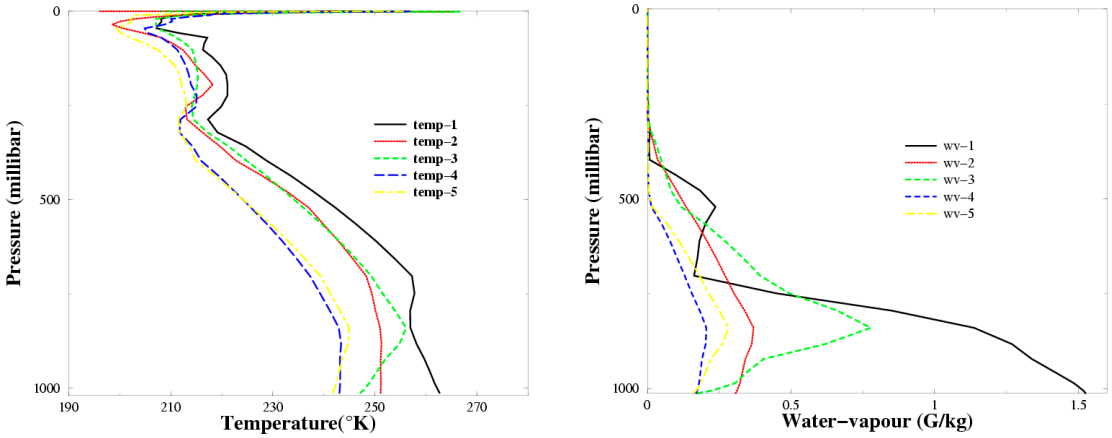

Figure 5. Temperature and humidity profiles used in the IASI brightness temperature simulations shown in Figures 3 and 4.

3.3. Simulated Cloudy IASI Spectra

Cloudy sky radiance spectra are simulated by using the Radiative Transfer model (RTX) [46–49]. RTX solves the radiative transfer equation with the adding and doubling method taking into account multiple scattering by randomly-oriented particles. Polarized radiation is considered in terms of Stokes parameters under the hypothesis of a plane-parallel and vertically inhomogeneous atmosphere including both thermal and solar sources. The spectral properties of atmospheric gases are computed with the Line-ByLine RadiativeTransfer Model (LBLRTM) model, while the extinction and scattering coefficients as well as the single scattering albedo and the Lagrange coefficients are computed for a gamma-modified size distribution of cloud particles (water and ice) using a Mie code [50]. The assumption of spherical ice particles in the near-IR through far-IR region is adopted here [51,52]. We assume this approximation as valid for the purpose of this study, although we are aware of implied limitations [53–56] that may affect polar radiative transfer in the presence of non-spherical ice particles. Future work will be dedicated to investigate the impact of this approximation on the cloud detection

performances. We set a fixed observing angle at 10 degrees off nadir, while other parameters are varied as indicated in Table 1. In particular, we considered spectral emissivity from three different surface types, clear and cloudy sky (three cloud phases), eight values for cloud particle effective radius (r_{eff}), seven different cloud top heights (CTH), and six different values for cloud liquid or ice water content (cwc). Using these different combinations, we obtained 1008 cloud simulated spectra for the three considered types of surface emissivity (ice, snow, and sea-water). The cloud geometrical thickness is 0.5 km for clouds with CTP = 5.2 and 5.7 km, 0.8 km for clouds with CTP = 3.2 and 3.7 km, and finally 1 km for clouds with CTP = 0.5, 2.2 and 2.7 km. We assume that the vertical profile of cloud parameters is homogeneous.

Table 1. List of parameters varied for producing the data set of high resolution infrared (IR) upwelling spectra.

Emissivity (ε_λ)	Ice, Snow and Sea-Water
Cloud Phase	Clear-sky, liquid, ice, and mixed phase
Cloud particle effective radius (r_{eff})	5, 10, 15, 20, 30, 50, 70, 100 μm
Ice or liquid water content (cwc)	0.001, 0.005, 0.01, 0.03, 0.05, 0.07 g/m^3
Cloud top (CTH)	0.5, 2.2, 2.7, 3.2, 3.7, 5.1, 5.5 km

The spectral emissivities (Figure 1) and the radiosonde temperature and humidity profiles (Figure 6) have been used to simulate the selected simulated spectra (Figures 7–10). The atmospheric profiles show an inversion strength of about 15 K and an evident dry layer at the inversion top. It is worth noticing that clear-sky conditions were reported during the radiosonde launch. Because of the inversion and the subsequent ambiguous temperature-height relationship, satellite observations at window channels would show about the same brightness temperature in clear sky or in the presence of a thick cloud top located at approximately 650 mb. Nevertheless, temperature inversions have been used in cloud detection algorithms as indicators of clear sky [20,57], as they can be detected by satellite infrared measurements using channels with weighting functions peaking in the lower troposphere. However, Holz and Ackerman [18] studied temperature inversions above the Arctic stratus and suggested that these cases could potentially confuse cloud detection based on the temperature inversion test only.

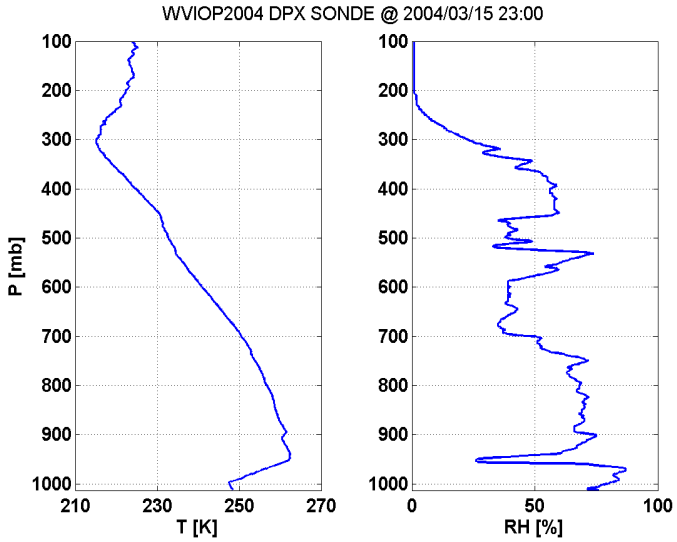

Figure 6. Radiosonde profile in the Arctic Winter used for the BT simulations shown in Figures 7–10. Simulated cloud tops were set at 0.5–2.2–2.7–3.2–3.7–5.1–5.5 km altitude, corresponding respectively to 947.60–757.30–707.87–661.03–616.53–503.99–475.22 mb pressure levels.

Figures 7 and 8 show clear and cloudy simulated BT spectra using ice surface emissivity with r_{eff} = 5 μm, two valu–es for cwc (0.01–0.05 g/m^3), and three values for CTH (2.2–2.7–0.5 km for water clouds and 3.7–3.2–0.5 km for ice clouds) in the presence of a water cloud and an ice cloud, respectively. Figures 9 and 10 are the same as Figures 7 and 8 but using sea-water surface emissivity. In the case of ice surface emissivity and water clouds, the slope decreases in the 750–1000 cm^{-1} range compared to clear sky, and BTs increase for all the used cloud tops and cwc combinations with respect to clear sky BTs (Figure 7). For ice emissivity and ice clouds, the slope and BTs in the 750–1000 cm^{-1} range may decrease or increase according to CTH and cwc compared to sea-water emissivity and clear sky. In particular, in the cases reported in Figure 8, BTs decrease when CTH = 3.7 km, and the slope decreases when CTH = 3.2 and 0.5 km. For sea-water emissivity and water clouds, BTs increase compared to clear sky BTs, but the slope changes according to CTH and cwc (Figure 9). As far as sea-water emissivity and ice clouds are concerned, the slope and BTs decrease or increase compared to clear sky BTs in the 750–1000 cm^{-1} range according to CTH and cwc (Figure 10). By comparing the results obtained using ice, snow, and sea-water emissivity both in clear and cloudy sky, it is evident that spectral features strictly related to the emissivity typical of polar surfaces are very similar to cloud spectral signatures, despite some minor differences. This analysis suggests that cloud detection techniques relying on thresholds cannot easily distinguish between clear-sky and cloudy cases. Both kinds of ice clouds and ice surface emissivity cause the slope to increase in the 750–1000 cm^{-1} range, and hence it is difficult to detect cloud presence on the basis of the window spectral region. Some ice clouds for instance cause the slope to increase when using sea-water emissivity (Figure 10), while they can cause the slope to decrease when using ice surface emissivity, according to microphysical cloud parameters (Figure 8).

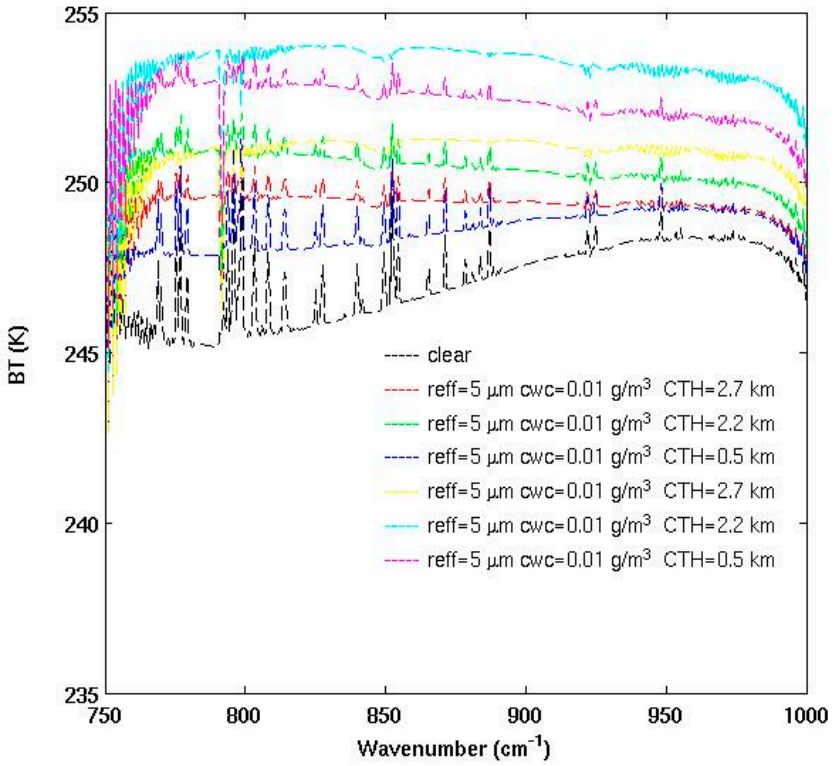

Figure 7. Simulated IASI brightness temperature spectra in clear and cloudy sky using ice surface emissivity. Water clouds with r_{eff} = 5 μm, cwc = 0.01 and 0.05 g/m^3, CTH = 2.2, 2.7, and 0.5 km.

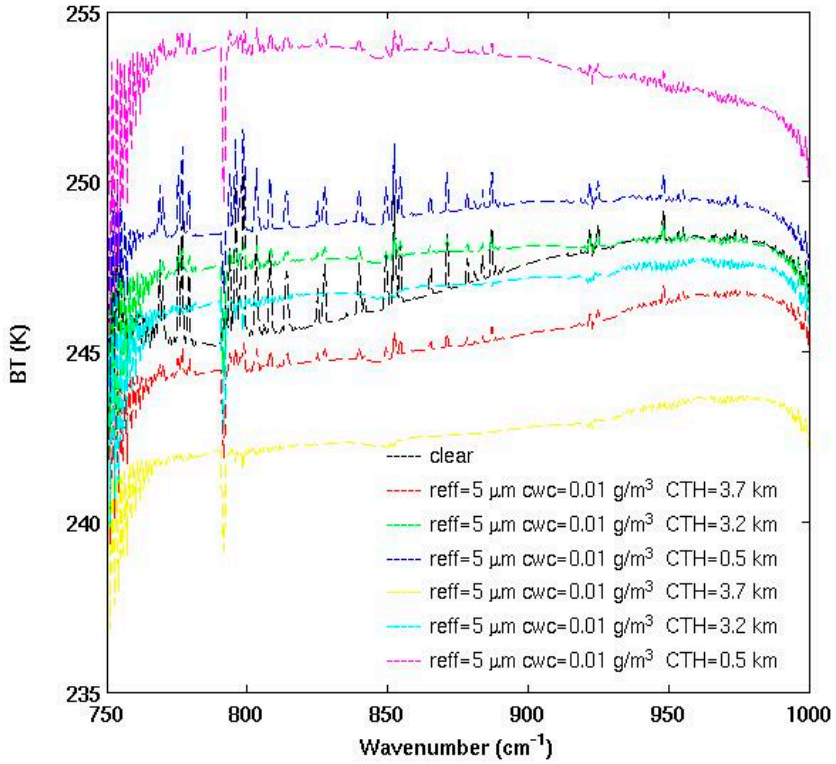

Figure 8. Simulated IASI brightness temperature spectra in clear and cloudy sky using ice surface emissivity. Ice clouds with r_{eff} = 5 µm, cwc = 0.01 and 0.05 g/m^3, CTH = 3.2, 3.7, and 0.5 km.

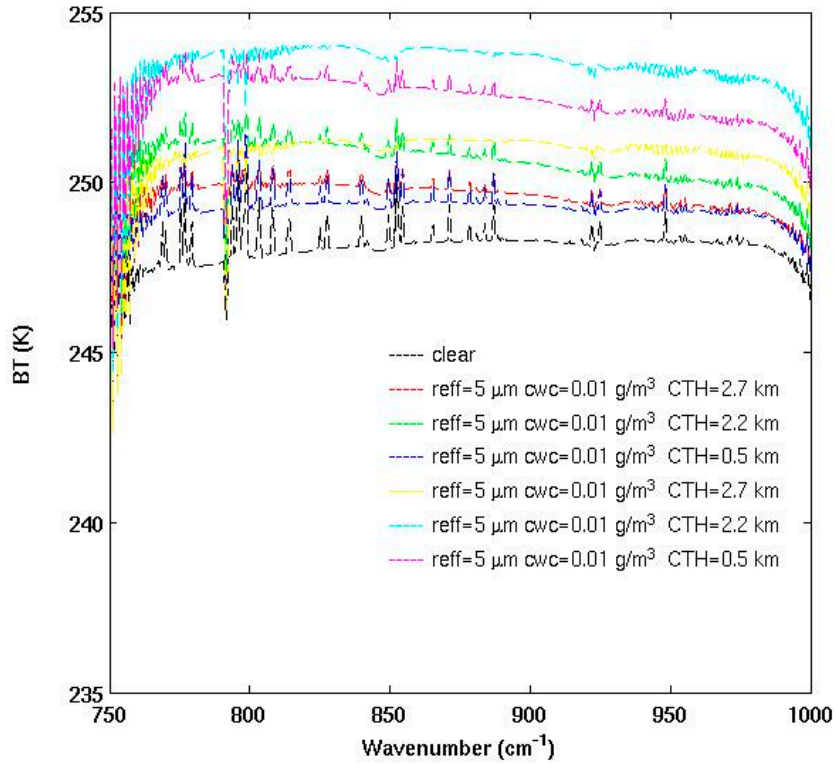

Figure 9. Simulated IASI brightness temperature spectra in clear and cloudy sky using sea-water surface emissivity. Water clouds with r_{eff} = 5 µm, cwc = 0.01 and 0.05 g/m^3, CTH = 2.2, 2.7, and 0.5 km.

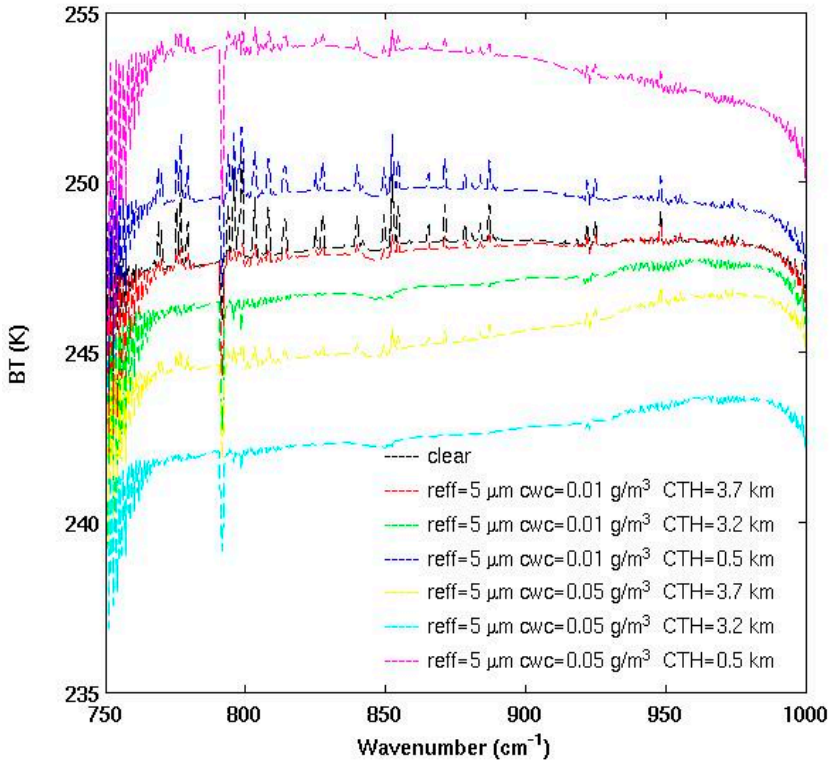

Figure 10. Simulated IASI brightness temperature spectra in clear and cloudy sky using sea-water surface emissivity. Ice clouds with r_{eff} = 5 µm, cwc = 0.01 and 0.05 g/m^3, CTH = 3.2, 3.7, and 0.5 km.

4. Arctic Cloud Detection

In this study, we analyse the IR window tests usually exploited in cloud detection schemes [16,17] over the Arctic region. These tests, listed in Table 2, have been adapted to work with IASI data. In order to understand the performance of the window IR threshold tests listed in Table 2, we applied them to the set of 305 simulated clear-sky spectra described in Section 3. Results are reported in Table 3. Table 3 shows that the tests in Table 2 are able to detect clear sky correctly only in the case of sea-water surface. Clear spectra are misidentified as cloudy when using ice or snow surfaces, because surface emissivity spectral features cause clear-sky BTs to resemble cloud signatures in the 750–1000 cm^{-1} range (Figure 3). These results confirm that night-time window IR threshold tests are not able to detect clear-sky spectra on ice and snow surfaces. We also applied the above-mentioned tests to the simulated cloudy spectra described in Section 3. The results are reported in Table 4. The tests misidentified "cloud-as-clear" for about 20–30% of the spectra, depending upon the surface emissivity used. In order to improve the capability of detecting clouds in the polar region, we examined the clear-sky spectral signal in the window region between 750–1000 cm^{-1}. We can see that the shape of the window spectrum remains the same when changing atmospheric profiles and using the same emissivity (Figures 3 and 4).

For evaluating the variability of the correlation between the simulated spectra, we computed the correlation coefficient between a reference clear IASI spectrum simulated with a fixed emissivity and 912 clear IASI spectra simulated using temperature and humidity profiles and ice, sea-water, and snow emissivity (as described in Section 3). In particular, for fixed ice emissivity the correlation coefficients are reported in Figure 11. The correlation coefficient estimation is restricted to a set of microwindows, centred at 787.5, 820.5, 874.0, and 960.0 cm^{-1} with a width of 5 cm^{-1}. These microwindows have been determined by minimizing the noise in order to give a sufficiently fine representation of the window shape.

Table 2. Cloud mask spectral tests (TEST IR).

Measured Inversion Strength	>10 K	Clear
BT800–BT1100	<−0.05	Ice cloud
	>1.0	Water cloud
BT960–BT1100	>1.0	Water cloud

Table 3. Percentage of simulated clear spectra detected incorrectly, over the entire set (305 Field of Views (FOVs) for each emissivity). The spectrum is declared clear if the correlation coefficient is greater than 0.98, otherwise it is declared as cloudy.

	IR Tests	Correlation Test
Emissivity	Percent of clear FOVs detected as cloudy (%)	Percent of clear FOVs detected as cloudy (%)
Ice	100	2
Snow	100	2
Sea-Water	15	0

Table 4. Percentage of simulated cloud spectra detected incorrectly over the entire set (1008 Field of Views (FOVs) for each emissivity).

	IR Tests	Correlation Test
Emissivity	Percent of cloudy FOVs detected as clear (%)	Percent of cloudy FOVs detected as clear (%)
Ice	20.2	0.9
Snow	28.1	7.6
Sea-Water	28.4	4.7

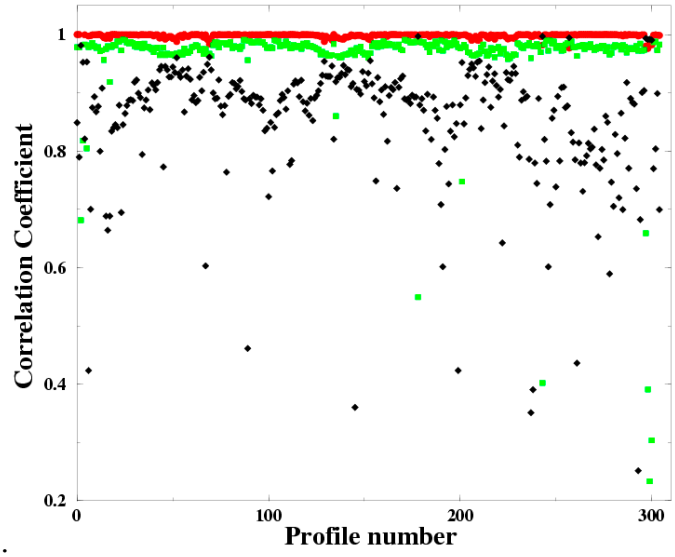

Figure 11. Correlation coefficient between an IASI spectrum simulated using ice emissivity and IASI spectra simulated using different temperatures and humidity profiles, and sea-water (black diamond), ice (red dot), and snow (green square) emissivities.

The calculation indicates that the correlation coefficient between different clear IASI spectra simulated with the same emissivity, but different temperature and humidity profiles, reaches values close to 1. In order to detect cloud and clear simulated spectra (as described in Section 3) we calculated the correlation coefficient between a fixed clear and the examined IASI spectra. If the correlation coefficient is greater than 0.98 the spectrum is declared clear, otherwise it is declared as cloudy. This threshold has been derived considering both simulated and measured IASI spectra for different emissivities.

Applying this correlation test (denominated Test 1 in the following) to the cloud simulated spectra, the number of cloudy spectra detected as clear decreases considerably with respect to the IR tests, and most of the clear spectra are detected correctly (Table 3).

In order to validate the correlation test with real data, we built a database with IASI clear spectra measured in the Arctic region including 500 night granule IASI l1c data from 1 November to 31 December 2008 between 55°N–75°N and 149°W–168°E. Of these granules, 400 are used for building the clear dataset, and the others for validating the algorithm. The emissivity has been derived from MOD11 surface products [58], and the MODIS product is derived from a physics-based day/night LST algorithm used to retrieve surface band emissivities and temperatures simultaneously from a pair of daytime and nighttime MODIS observations in 20, 22, 23, 29, and 31–33 channels over all types of land cover. The clear IASI spectra are identified by using 2B-GEOPROF-LIDAR products. The correlation coefficients for Test 1 have been computed between the examined IASI spectrum and a restricted set of spectra selected among the measured clear IASI database according to the surface and satellite zenith angle. If the correlation coefficient (Test 1) is below a certain dynamic threshold [59] the spectrum is identified as cloudy, while if the correlation test is successful, the spectrum in analysis undergoes the following additional tests in order to estimate if it is clear or partially cloudy. The correlation for sea-water surface (Figure 11) and also for other non-heterogeneous surfaces is much lower, and consequently the test works less well. For this reason, these three other tests have been added to detected cloudy FOVS.

Test 2 is the shortwave-longwave (SW-LW) window test. This test uses brightness temperatures of two IASI atmospheric window channels, one in the shortwave (SW) region at 2558.224 cm^{-1} and the other in the longwave (LW) region at 903.5 cm^{-1}. The field of view is clear if the difference between the two channels remains within the predetermined dynamic thresholds e_{1a} and e_{1b} [59].

Test 3 is the shortwave-longwave (SW LW) test. A set of 92 IASI channels in the LW region are used to predict the IASI channel at 2525.130 cm^{-1} in the SW. The regression analysis is done with a least square stepwise backward glance technique [60]. The code used for the regression is RLSTP on the International Mathematical and Statistical Library (IMSL) [61]. The best predictors are extracted from the first 1421 IASI SW channels and they are found to be the same for all the scanning angles. The selected 92 predictors explain more than 99.99% of the total variance. The field of view is defined as clear if the difference between the predicted and observed brightness temperatures is within fixed dynamic thresholds e_{1a} and e_{1b}.

Test 4 is the Window spatial variability test. This final test is based on one IASI LW window channel (903.5 cm^{-1}). For each FOV, the brightness temperature at this channel is compared with the BT values of the surrounding FOVs (3×3 box), corresponding to similar characteristics in terms of surface type and orography. If the brightness temperature of the central FOV is colder than the values of surrounding FOVs by more than a selected threshold, the central FOV is categorized as cloudy. These tests were also used with success in the Atmospheric Infrared Sounder (AIRS) cloud detection [59]. The IASI FOV is classified as clear if at least one of the tests in the sequence 2 to 4 is successful, otherwise the FOV is classified as partially cloudy.

The dynamic thresholds are obtained from the use of the measured and simulated clear-sky datasets. Simulated data provide a useful estimate of the variability of the threshold values around the mean value that should be exploited. In this approach, the difference between the predicted and measured channel brightness temperatures is assumed to be within a range, whose medium value is calculated from the measured data, while the boundaries (minimum and maximum) are estimated from the simulated data. The cloud detection scheme selects the dynamic threshold values and the test coefficients according to the satellite zenith angle, land cover, and the maximum spectrum brightness temperature [59].

5. Validation of Cloud Detection

The validation of the arctic cloud detection algorithm was carried out on the basis of spatial and temporal co-located products from 2B-GEOPROF-LIDAR and the Advanced Very High Resolution

Radiometer (AVHRR/3). The first step considers the 2B-GEOPROF-LIDAR product within the IASI FOV; if this contains both clear and cloudy 2B-GEOPROF-LIDAR pixels, the IASI FOV is classified as "partially cloudy", otherwise the procedure goes to the next step. Thus, the second step is reached only if the 2B-GEOPROF-LIDAR pixels are all either clear or cloudy, though this information cannot be extended to the IASI FOVs, since IASI FOVs are always larger than the area covered by the 2B-GEOPROF-LIDAR product. Let us note that the CPR footprint is approximately 2.5 km (along track) by 1.4 km (across-track), while the IASI FOV size is 12 km at nadir. The CloudSat/CPR overlaps IASI FOVS along a diagonal, so that the IASI FOV is never completely covered by the CPR pixels. The number of pixels along the CloudSat/CALIPSO track within the IASI footprint depends on the satellite view angle. Figure 12 shows one IASI spectrum and the 2B-GEOPROF-LIDAR cloud profiling product co-located on the IASI footprint for a high cloud.

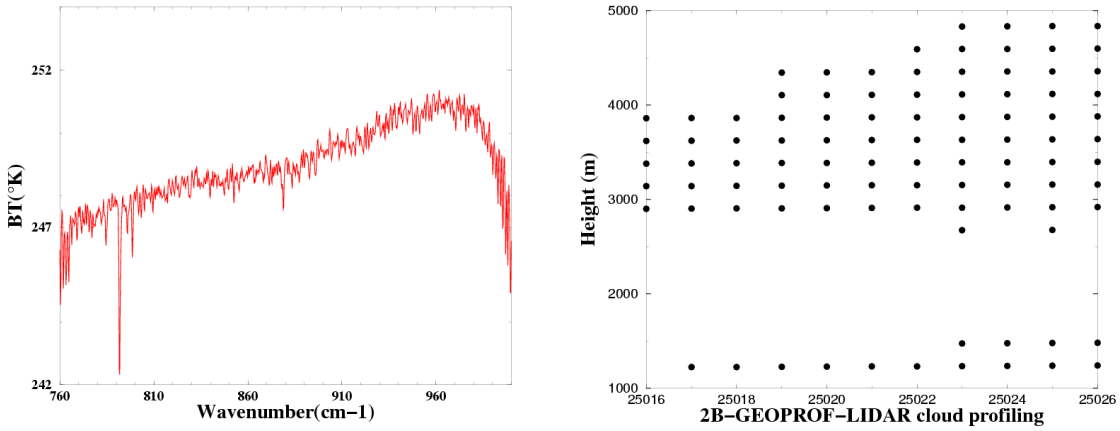

Figure 12. Left: IASI observations while looking at a thick high cloud deck. Right: Cloud Geometrical Profile from combined CPR and CALIPSO Lidar (2B-GEOPROF-LIDAR) cloud profiling colocated within the IASI footprint; each point indicates the presence of clouds at height level (y axis) and 2B-GEOPROF-LIDAR pixel number (x axis).

In the second step, the homogeneity of the IASI FOVs is investigated by using simultaneous AVHRR data within the IASI FOVs. The homogeneity criterion is satisfied when all the AVHRR/3 FOVs co-located on the IASI FOV are either clear or cloudy, then the IASI FOV is classified as "clear" or "cloudy" according to the 2B-GEOPROF-LIDAR product (all either clear or cloudy). If the homogeneity criterion is not satisfied, then the IASI FOV is classified as "partially cloudy". It is worth noting that the Mask AVHRR for Inversion ATOVS (MAIA) cloud detection [62] has been used to classify AVHRR FOVs. The performances for tests 1 to 4 (denominated TS1–4 tests from now onwards) and for the IR tests are described in terms of probability of detection and misidentification rates. We define N10 as the number of cloudy cases misidentified as clear (misses) and N01 the number of clear cases misidentified as cloudy (false). N11 and N00 corresponds to the number of cases correctly identified as cloudy and clear, respectively. Using these numbers we define the accuracy (A), the probability of detection (POD), the false alarm ratio (FAR), and the Hansen Kuipers discriminant (HK) as the following:

$$A = (N11 + N00)/(N11 + N00 + N01 + N10)$$
$$POD = N11/(N10 + N11)$$
$$FAR = N01/(N11 + N01)$$
$$HK = (N11/(N11 + N10)) - (N01/(N01 + N00))$$

In Table 5 we report the performances, in terms of probability of detection and misidentification rates, of three cloud detection algorithms: TS1–4, the IR tests, and the tests exploited in the MODIS collection 6 (C6) for polar night-time cloud detection [24,26]. For homogeneous IASI FOVs, the TS1–4 tests tally with 2B-GEOPROF-LIDAR in classifying 97.54% of clear FOVs as clear and also in classifying

98.11% of cloudy FOVs as cloudy. The probability of cloud detection POD is 98.10%, while the false alarm ratio FAR is 1.23% and the HK discriminant reaches 0.95. For homogeneous IASI FOVs, the IR tests tally with 2B-GEOPROF-LIDAR in classifying 67.11% of clear FOVs as clear and 70.91% of cloudy FOVs as cloudy; POD is 70.91%, while the false alarm ratio is 18.79% and the HK discriminant is 0.38. Tables 6 and 7 show the performance of the TS1–4, IR tests, and MODIS C6 in terms of probability of detection and misidentification rates for clouds with the optical depth smaller or larger than three, respectively. The cloud optical depth, the 2B-TAU product, is distributed by the CloudSat data processing centre (http://cloudsat.atmos.colostate.edu/). The 2B-TAU product is based on MODIS radiance data, CPR reflectivity and other ancillary data (e.g., geolocation, surface albedo, and time). The cloud optical depth (COD) has been estimated only for completely covered homogeneous IASI FOVS, and the homogeneity is investigated by AVHRR. If the 2B-GEOPROF-LIDAR COD is the same for the all pixels within the IASI footprint, we suppose that it is the same for the whole IASI FOV. For a cloud optical depth smaller than three, the TS1–4 tests tally with 2B-GEOPROF-LIDAR in classifying 97.89% of cloudy FOVs as cloudy. For a cloud optical depth greater than three the TS1–4 tests classify 98.15% of cloudy FOVs correctly. Therefore, the tests confirm good performances for thin clouds also. The IR tests tally with 2B-GEOPROF-LIDAR in classifying 67.16% and 71.49% of cloudy FOVs as cloudy respectively for cloud optical smaller or larger than three. For non-homogenous partially cloudy IASI FOVs, the TS1–4 tests detect 88.5% of FOVs correctly (Table 8). Judging from the 2B-GEOPROF-LIDAR product, by visual inspection of several cases, the lower score in partially cloudy cases is typically due to low broken clouds that are not often identified correctly by the tests. Nonetheless, the TS1–4 tests together with dynamic land cover information considerably increase the accuracy of the cloud mask when compared to the IR tests.

Table 5. Statistics for the window IR tests, theTS1–4 proposed tests, and the Moderate–Resolution Imaging Spectroradiometer MODIS collection C6 tests considering the homogenous Field of Views (FOVs). Number of total FOVs: 2932; number of cloudy FOVs: 1956; number of clear FOVs: 976. N00: number of cases correctly identified as clear. N11: number of cases correctly identified as cloudy. N01: number of clear cases misidentified as cloudy. N10: number of cloudy cases misidentified as clear. A; accuracy, POD: probability of detection, FAR: the false alarm ratio, HK: Hansen Kuipers discriminant.

	IR Tests	**MODIS C6 Tests**	**TS1–4 Tests**
Percent of clear FOVs detected as clear (%)	67.11	84.03	97.54
Percent of cloudy FOVs detected as cloudy (%)	70.91	88.80	98.11
N00	655	821	952
N11	1387	1736	1919
N01	321	156	24
N10	569	219	37
A (%)	69.74	87.21	98.05
POD (%)	70.91	88.79	98.10
FAR (%)	18.79	8.24	1.23
HK	0.38	0.73	0.95

Table 6. Statistics for the IR, TS1–4, and MODIS C6 tests considering cloudy Field of Views (FOVs) having an optical depth smaller than 3. Number of cloudy FOVs: 332. N11: number of cases correctly identified as cloudy. N10: number of cloudy cases misidentified as clear.

	IR Tests	**MODIS C6 Tests**	**TS1–4 Tests**
Percent of cloudy FOVs detected as cloudy (%)	67.16	84.04	97.89
N11	223	279	325
N10	109	43	7

Table 7. Statistics for the IR, TS1–4, and MODIS C6 tests considering cloudy Field of Views (FOVs) having an optical depth greater than 3. Number of cloudy FOVs: 1624. N11: number of cases correctly identified as cloudy. N10: number of cloudy cases misidentified as clear.

	IR Tests	MODIS C6 Tests	TS1–4 Tests
Percent of cloudy FOVs detected as cloudy (%)	71.49	85.16	98.15
N11	1161	1383	1594
N10	463	241	30

Table 8. Percentage of IASI Field of Views (FOVs) exactly detected considering the non-homogenous FOVs, (partially cloudy). Number of total partially cloudy FOVs: 1484.

	TS1–4 Tests
Percent of partially cloudy FOVs exactly detected (%)	88.5
Percent of partially cloudy FOVs detected as cloudy (%)	3.3
Percent of partially cloudy FOVs detected as clear (%)	8.2

6. Conclusions

This work reports on the results obtained investigating the effect of surface emissivity on polar night-time cloud detection algorithms. Based on a simulated dataset of IR upwelling radiation spectra with different emissivities, cloud phases, optical depths, and particle effective radii and shapes, we find that uncertainties in surface emissivity play a dominant role in the performances of the window threshold test often used in cloud detection during the night. In fact, clear-sky spectra computed by using typical polar surface emissivities do resemble cloud signatures, especially in the 750–1000 cm^{-1} range. This causes inaccuracy when using cloud detection techniques relying on thresholds (e.g., BT(11 μm)–BT(12 μm) test). As such, the performances of polar night-time cloud detection algorithms based on IASI simulated data show relatively low "cloudy-as-clear" but large "clear-as-cloudy" misidentification rates. This suggests that detection techniques relying on thresholds are appropriate for definite areas with well-known and/or stable surface emissivity, but the same threshold may not be exported to other polar areas with different characteristics. The cloud detection tests proposed here are able to detect cloudy IASI FOVs in the Arctic region, for different and complex surface types. For homogenous IASI FOVs, the cloud detection scheme tallies with combined radar-lidar detection (2B-GEOPROF-LIDAR) in correctly classifying 98.11% of FOVs as cloudy and also in correctly classifying 97.54% of FOVs as clear. The probability of cloud detection (POD) is 98.10% and the false alarm (FAR) is 1.23 and the HK discriminant reaches 0.95. For non-homogenous partially cloudy IASI FOVs, the cloud detection scheme detects 88.5% of FOVs correctly. For cloud optical depths smaller than three, the cloud detection scheme classifies 98.15% of FOVs correctly. Therefore, the cloud detection tests proposed also confirm good performances for thin clouds. This lower score is found to be caused by the presence of low broken clouds that are often identified incorrectly. The proposed tests together with dynamic emissivity information derived from MODIS products considerably increase the capacity to detect clouds during the polar night with respect to the other tests available in the open literature. Future work will be dedicated to investigate in more detail the cases of misdetection. In particular, it is interesting to study the impact of the emissivity variability within the IASI FOV and the effect of rapidly changing emissivity conditions due to events on shorter time-scales than the 16-day MODIS surface emissivity product.

Author Contributions: Filomena Romano and Domenico Cimini designed the research, wrote the paper and contributed to validation process. Saverio T. Nilo , Francesco Di Paola , Elisabetta Ricciardelli, Ermann Ripepi and Mariassunta Viggiano contributed to data processing, analysis and validation process. All the co-authors helped to revise the manuscript.

Conflicts of Interest: The authors declare no conflict of interest.

References

1. Illingworth, A.J.; Barker, H.W.; Beljaars, A.; Ceccaldi, M.; Chepfer, H.; Clerbaux, N.; Cole, J.; Delanoë, J.; Domenech, C.; Donovan, D.P. The EarthCARE satellite the next step forward in global measurements of clouds, aerosols, precipitation, and radiation. *BAMS* **2015**, *96*, 1311–1332. [CrossRef]
2. Kay, J.E.; L'Ecuyer, T.; Chepfer, H.; Loeb, N.; Morrison, A.; Cesana, G. Recent Advances in Arctic Cloud and Climate Research. *Curr. Clim. Chang. Rep.* **2016**, *2*, 159. [CrossRef]
3. Kay, J.E.; Bourdages, L.; Chepfer, H.; Miller, N.; Morrison, A.; Yettella, V.; Eaton, B. Evaluating and improving cloud phase in the community atmosphere model version 5 using spaceborne lidar observations. *J. Geophys. Res.* **2016**, *121*, 4162–4176. [CrossRef]
4. Morrison, H.; de Boer, G.; Feingold, G.; Harrington, J.Y.; Shupe, M.D.; Sulia, K. Resilience of persistent Arctic mixed-phase clouds. *Nat. Geosci.* **2012**, *5*, 11–17. [CrossRef]
5. Taylor, P.C.; Kato, S.; Xu, K.-M.; Cai, M. Covariance between Arctic sea ice and clouds within atmospheric state regimes at the satellite footprint level. *J. Geophys. Res. Atmos.* **2015**, *120*, 12656–12678. [CrossRef] [PubMed]
6. Bennartz, R.; Shupe, M.D.; Turner, D.D.; Walden, V.P.; Steffen, K.; Cox, C.J.; Kulie, M.S.; Miller, N.B.; Pettersen, C. Greenland melt extent enhanced by low-level liquid clouds. *Nature* **2013**, *496*, 83–86. [CrossRef] [PubMed]
7. Curry, J.A.; Rossow, W.B.; Randall, D.; Schramm, J.L. Overview of Arctic cloud and radiation characteristics. *J. Clim.* **1996**, *9*, 1731–1764. [CrossRef]
8. Schweiger, A.J.; Lindsay, R.W.; Key, J.R.; Francis, J.A. Arctic Clouds in Multiyear Satellite Data Sets. *Geophys. Res. Lett.* **1999**, *26*, 1845–1848. [CrossRef]
9. Boucher, O.; Randall, D.D.; Artaxo, P.; Bretherton, C.; Feingold, G.; Forster, P.; Kerminen, V.-M.; Kondo, Y.; Liao, H.; Lohmann, U.; et al. Clouds and aerosols. In *Climate Change 2013: The Physical Science Basis. Contribution of Working Group I to the Fifth Assessment Report of the Intergovernmental Panel on Climate Change*; Stocker, T.F., Qin, D., Plattner, G.-K., Tignor, M., Allen, S.K., Doschung, J., Nauels, A., Xia, Y., Bex, V., Midgley, P.M., Eds.; Cambridge University Press: Cambridge, UK, 2013; pp. 571–657.
10. Heidinger, A.; Li, Y.; Baum, B.; Holz, R.; Platnick, S.; Yang, P. Retrieval of Cirrus Cloud Optical Depth under Day and Night Conditions from MODIS Collection 6 Cloud Property Data. *Remote Sens.* **2015**, *7*, 7257–7271. [CrossRef]
11. Welch, R.M.; Feind, R.E.; Berendes, D.; Berendes, T.A.; Kuo, K.E.; Logar, A.M. The ASTER Polar Cloud Mask Algorithm Theoretical Basis Document, 1999. Available online: http://eospso.gsfc.nasa.gov//eos_homepage/for_scientists/atbd/docs/ASTER/atbd-ast-13.pdf (accessed on 13 February 2017).
12. Karlsson, K.-G.; Dybbroe, A. Evaluation of Arctic cloud products from the EUMETSAT Climate Monitoring Satellite Application Facility based on CALIPSO-CALIOP observations. *Atmos. Chem. Phys.* **2010**, *10*, 1789–1807. [CrossRef]
13. Rossow, W.B.; Garder, L.C.; Lacis, A.A. Global, seasonal cloud variations from satellite radiance measurements. Part I: Sensitivity of analysis. *J. Clim.* **1989**, *2*, 419–458. [CrossRef]
14. Stowe, L.L.; Yeh, H.Y.M.; Eck, T.F.; Wellemeyer, C.G.; Kyle, H.L. The Nimbus-7 Cloud Data Processing Team Nimbus-7 global cloud climatology. Part II: First year results. *J. Clim.* **1989**, *2*, 671–709. [CrossRef]
15. Liu, Y.; Ackerman, S.A.; Maddux, B.C.; Key, J.R.; Frey, R.A. Errors in Cloud Detection over the Arctic Using a Satellite Imager and Implications for Observing Feedback Mechanisms. *J. Clim.* **2010**, *23*, 1894–1907. [CrossRef]
16. IASI Level 2 Product Guide: EUM/OPSEPS/MAN/04/0033, EUMETSAT. Available online: www.eumetsat.int (accessed on 15 December 2016).
17. Ackerman, S.A.; Strabala, K.I.; Menzel, W.P.; Frey, R.A.; Moeller, C.C.; Gumley, L.I. Discriminating clear-sky from clouds with MODIS. *J. Geophys. Res.* **1998**, *103*, 32141–32158. [CrossRef]
18. Holz, R.E.; Ackerman, S.A. Arctic Winter High Spectral Resolution Cloud Height Retrievals. In Proceedings of the Conference on Satellite Meteorology and Oceanography, Atlanta, GA, USA, 29 January–2 February 2006.
19. Holz, R.E.; Ackerman, S.A.; Nagle, F.W.; Frey, R.; Dutcher, S.; Kuehn, R.E.; Vaughan, M.A.; Baum, B. Global Moderate Resolution Imaging Spectroradiometer (MODIS) cloud detection and height evaluation using CALIOP. *J. Geophys. Res.* **2008**, *113*, D00A19. [CrossRef]

20. Liu, Y.; Key, J.R.; Frey, R.A.; Ackerman, S.A.; Menzel, W.P. Night Time Polar Cloud Detection with MODIS. *Remote Sens. Environ.* **2004**, *92*, 181–194. [CrossRef]
21. Ackerman, S.A.; Holz, R.E.; Frey, R.A.; Eloranta, E.W.; Maddux, B.C.; McGill, M. Cloud detection with MODIS. Part II: Validation. *J. Atmos. Ocean. Technol.* **2008**, *25*, 1073–1086. [CrossRef]
22. Frey, R.A.; Ackerman, S.A.; Liu, Y. Cloud detection with MODIS. Part I: Improvements in the MODIS cloud mask for collection 5. *J. Atmos. Ocean. Technol.* **2008**, *25*, 1057E–1072E. [CrossRef]
23. King, M.D.; Platnick, S.; Menzel, W.P.; Ackerman, S.A.; Hubanks, P.A. Spatial and Temporal Distribution of Clouds Observed by MODIS Onboard the Terra and Aqua Satellites. *IEEE Trans. Geosci. Remote Sens.* **2013**, *51*, 3826–3852. [CrossRef]
24. Baum, B.A.; Menzel, W.P.; Frey, R.A.; Tobin, D.C.; Holz, R.E.; Ackerman, S.A. MODIS Cloud-Top Property Refinements for Collection 6. *J. Appl. Meteorol. Clim.* **2012**, *51*, 1145–1163. [CrossRef]
25. Hutchison, K.D.; Iisager, B.D.; Mahoney, R.L. Enhanced snow and ice identification with the VIIRS cloud mask algorithm. *Remote Sens. Lett.* **2013**, *4*, 929–936. [CrossRef]
26. Platnick, S. *MODIS Cloud Optical Properties: User Guide for the Collection 6 Level-2 MOD06/MYD06 Product and Associated Level-3 Datasets*; NASA Goddard: Greenbelt, MD, USA, 2014; p. 141.
27. Liang, C.K.; Mills, S.; Hauss, B.I.; Miller, S.D. Improved VIIRS Day/Night Band Imagery with Near-Constant Contrast. *TGRS* **2014**, *52*, 11. [CrossRef]
28. Walther, A.; Heidinger, A.K.; Miller, S. The expected performance of cloud optical and microphysical properties derived from Suomi NPP VIIRS day/night band lunar reflectance. *J. Geophys. Res. Atmos.* **2013**, *118*, 230–240. [CrossRef]
29. Masiello, G.; Serio, C.; Cuomo, V. Exploiting quartz spectral signature for the detection of cloud-affected satellite infrared observations over African desert areas. *Appl. Opt.* **2004**, *43*, 2305–2315. [CrossRef] [PubMed]
30. Klaes, K.D.; Cohen, M.; Buhler, Y.; Schlüssel, S.; Munro, R.; Luntama, J.P.; Von Engeln, A.; Clerigh, E.O.; Bonekamp, H.; Ackermann, J.; et al. An introduction to the EUMETSAT Polar System. *Bull. Am. Meteorol. Soc.* **2007**, *88*, 1085–1096. [CrossRef]
31. Aires, F.; Rossow, W.B.; Scott, N.A.; Chédin, A. Remote Sensing from the infrared atmospheric sounding interferometer instrument 2. Simultaneous retrieval of temperature, water vapor and ozone atmospheric profiles. *J. Geophys. Res.* **2002**, *107*, 4620–4631. [CrossRef]
32. Ricciardelli, E.; Romano, F.; Cuomo, V. Physical and statistical approaches for cloud identification using Meteosat Second Generation-Spinning Enhanced Visible and Infrared Imager Data. *Remote Sens. Environ.* **2008**, *112*, 2741–2760. [CrossRef]
33. Stephens, G.L.; Vane, D.G.; Boain, R.J.; Mace, G.G.; Sassen, K.; Wang, Z.; Illingworth, A.J.; O'Connor, E.J.; Rossow, W.B.; Durden, S.L.; et al. The CloudSat mission and the A-train. *B. Am. Meteor. Soc.* **2002**, *83*, 1771–1790. [CrossRef]
34. Mace, G.G.; Marchand, R.; Zhang, Q.; Stephens, G. Global hydrometeor occurrence as observed by CloudSat: Initial observations from Summer. *Geophys. Res. Lett.* **2006**, *34*, L09808.
35. Marchand, R.; Mace, G.G.; Ackerman, T.; Stephens, G. Hydrometeor Detection Using CloudSat—An Earth-Orbiting 94-GHz Cloud Radar. *J. Atmos. Ocean. Technol.* **2008**, *25*, 519–533. [CrossRef]
36. Winker, D.M.; Pelon, J.; McCormick, M.P. The CALIPSO mission: Spaceborne lidar for observation of aerosols and clouds. *Proc. SPIE* **2003**, *4893*, 1–11.
37. You, Y.; Kattawar, G.W.; Yang, P.; Hu, Y.X.; Baum, B.A. Sensitivity of depolarized lidar signals to cloud and aerosol particle properties. *J. Quant. Spectrosc. Radiat. Transf.* **2006**, *100*, 470–482. [CrossRef]
38. Li, Z.L.; Becker, F.; Stoll, M.P.; Wan, Z. Evaluation of six methods for extracting relative emissivity spectra from thermal IR images. *Remote Sens. Environ.* **1999**, *69*, 197–214. [CrossRef]
39. Hale, G.M.; Querry, M.R. Optical Constants of Water in the 200-nm to 200-µm. Wavelength Region. *Appl. Opt.* **1973**, *12*, 555–563. [CrossRef] [PubMed]
40. Warren, S.G. Optical constants of ice from the ultraviolet to the microwave. *Appl. Opt.* **1984**, *23*, 1206–1225. [CrossRef] [PubMed]
41. Chevallier, F.; Chéruy, F.; Scott, N.A.; Chédin, A. A neural network approach for a fast and accurate computation of longwave radiative budget. *J. Appl. Meteorol.* **1998**, *37*, 1385–1397. [CrossRef]
42. Westwater, E.R.; Cimini, D.; Mattioli, V.; Gasiewski, A.J.; Klein, M.; Leuski, V.; Liljegren, J.C. The 2004 North Slope of Alaska Arctic Winter Radiometric Experiment: Overview and Recent Results. In Proceedings of the ARM Science Team Meeting, Albuquerque, NM, USA, 27–31 March 2006.

43. Ackerman, T.P.; Stokes, G.; Wiscombe, W.; Turner, D. The Atmospheric Radiation Measurement Program: First 20 Years. Available online: http://journals.ametsoc.org/toc/amsm/57 (accessed on 13 February 2017).
44. Verlinde, J.; Zak, B.D.; Shupe, M.D.; Ivey, M.D.; Stamnes, K. The ARM North Slope of Alaska (NSA) sites. *Meteorol. Monogr.* **2016**. [CrossRef]
45. Clough, S.A.; Shephard, M.W.; Mlawer, E.J.; Delamere, J.S.; Iacono, M.J.; Cady-Peirera, K.; Boukabara, S.; Brown, P.D. Atmospheric radiative transfer modeling: A summary of AER codes. *J. Quant. Spectrosc. Radiat. Transf.* **2005**, *91*, 233–244. [CrossRef]
46. Evans, K.F.; Stephens, G.L. A new polarized atmosphere radiative transfer model. *J. Quant. Spectrosc. Radiat. Transf.* **1991**, *46*, 412–423. [CrossRef]
47. Rizzi, R.; Smith, J.A.; Di Pietro, P.; Loffredo, G. Comparison of modelled and measured stratus cloud infrared spectral signatures. *J. Geophys. Res.* **2001**, *106*, 34109–34119. [CrossRef]
48. Amorati, R.; Rizzi, R. Radiances simulated in the presence of clouds by use of a fast radiative transfer model and a multiple-scattering scheme. *Appl. Opt.* **2002**, *41*, 1604–1614. [CrossRef] [PubMed]
49. Maestri, T.; Rizzi, R.; Smith, J.A. Spectral infrared analysis of a cirrus cloud based on Airborne Research Interferometer Evaluation System (ARIES) measurements. *J. Geophys. Res.* **2005**, *110*, D06111. [CrossRef]
50. Wiscombe, W.J. *NCAR Technical Note, NCAR/TN-140+STR*; National Centre for Atmospheric Research: Boulder, CO, USA, 1979.
51. Grenfell, T.C.; Warren, S.G. Representation of a non-spherical ice particle by a collection of independent spheres for scattering and absorption of radiation. *J. Geophys. Res.* **2010**, *104*, 697–709.
52. Mahesh, A.; Walden, V.P.; Warren, S. Ground-based remote sensing of cloud properties over the Antarctic Plateau. Part II: Cloud optical depths and particle sizes. *J. Appl. Meteorol.* **2001**, *40*, 1279–1294. [CrossRef]
53. Yang, P.; Bi, L.; Baum, B.A.; Liou, K.-N.; Kattawar, G.W.; Mishchenko, M.I.; Cole, B. Spectrally consistent scattering, absorption, and polarization properties of atmospheric ice crystals at wavelengths from 0.2 to 100 µm. *J. Atmos. Sci.* **2013**, *70*, 330–347. [CrossRef]
54. Yang, P.; Wei, H.; Huang, H.-L.; Baum, B.A.; Hu, Y.X.; Kattawar, G.W.; Mishchenko, M.I.; Fu, Q. Scattering and absorption property database for nonspherical ice particles in the near-through far-infrared spectral region. *Appl. Opt.* **2005**, *44*, 5512–5523. [CrossRef] [PubMed]
55. Baum, B.A.; Yang, P.; Heymsfield, A.J.; Bansemer, A.; Cole, B.H.; Merrelli, A.; Schmitt, C.; Wang, C. Ice cloud single-scattering property models with the full phase matrix at wavelengths from 0.2 to 100 mm. *J. Quant. Spectrosc. Radiat. Transf.* **2014**, *146*, 123–139. [CrossRef]
56. Emde, C.; Buras-Schnell, R.; Kylling, A.; Mayer, B.; Gasteiger, J.; Hamann, U.; Kylling, J.; Richter, B.; Pause, C.; Dowling, T.; et al. The libRadtran software package for radiative transfer calculations (version 2.0.1). *Geosci. Model Dev.* **2016**, *9*, 1647–1672. [CrossRef]
57. Ackerman, S.A. Global Satellite Observations of Negative Brightness Temperature Differences between 11 and 6.7 µm. *J. Atmos. Sci.* **1996**, *53*, 2803–2812. [CrossRef]
58. Wan, Z. MODIS Land Surface Temperature Products Users' Guide. 2009. Available online: https://icess.eri.ucsb.edu/modis/LstUsrGuide/usrguide.html (accessed on 13 February 2017).
59. Romano, F.D.; Cimini, D.; Rizzi, R.; Cuomo, V. Multilayered cloud parameters retrievals from combined infrared and microwave satellite observations. *J. Geophys. Res.* **2007**, *112*, D08210. [CrossRef]
60. Efroymson, M.A. Multiple regression analysis. In *Mathematical Methods for Digital Computers*; Ralston, A., Wilf, H., Eds.; John Wiley & Sons: New York, NY, USA, 1960; pp. 191–203.
61. International Mathematical and Statistical Library. *User's Manual. IMSL Library, Fortran Subroutines for Mathematics and Statistics*; International Mathematical and Statistical Library: Houston, TX, USA, 1999; Available online: http://docs.roguewave.com/imsl/fortran/7.0/math/math.pdf (accessed on 13 February 2017).
62. Lavanant, L. MAIA AVHRR Cloud Mask and Classification. EUMETSAT Contract Documentation Ref. MF/DP/CMS/R&D/MAIA3, 2002. Available online: www.meteorologie.eu.org/ici/maia/maia3.pdf (accessed on 13 February 2017).